LLNL-PROC-561298

LAWRENCE
LIVERMORE
NATIONAL
LABORATORY

Experimental techniques for measuring Rayleigh-Taylor instability in inertial confinement fusion (ICF)

V. A. Smalyuk

June 14, 2012

Turbulent Mixing and Beyond 2011
Trieste, Italy
August 21, 2011 through August 28, 2011

Disclaimer

This document was prepared as an account of work sponsored by an agency of the United States government. Neither the United States government nor Lawrence Livermore National Security, LLC, nor any of their employees makes any warranty, expressed or implied, or assumes any legal liability or responsibility for the accuracy, completeness, or usefulness of any information, apparatus, product, or process disclosed, or represents that its use would not infringe privately owned rights. Reference herein to any specific commercial product, process, or service by trade name, trademark, manufacturer, or otherwise does not necessarily constitute or imply its endorsement, recommendation, or favoring by the United States government or Lawrence Livermore National Security, LLC. The views and opinions of authors expressed herein do not necessarily state or reflect those of the United States government or Lawrence Livermore National Security, LLC, and shall not be used for advertising or product endorsement purposes.

Experimental techniques for measuring Rayleigh–Taylor instability in inertial confinement fusion (ICF)

V. A. Smalyuk

Lawrence Livermore National Laboratory

Livermore, California 94551 USA

Rayleigh–Taylor (RT) instability is one of the major concerns in inertial confinement fusion (ICF) because it amplifies target modulations in both acceleration and deceleration phases of implosion, which leads to shell disruption and performance degradation of imploding targets. This article reviews experimental results of the RT growth experiments performed on OMEGA laser system, where targets were driven directly with laser light. RT instability was studied in the linear and nonlinear regimes. The experiments were performed in acceleration phase, using planar and spherical targets, and in deceleration phase of spherical implosions, using spherical shells. Initial target modulations consisted of 2-D pre-imposed modulations, and 2-D and 3-D modulations imprinted on targets by the non-uniformities in laser drive. In planar geometry, the nonlinear regime was studied using 3-D modulations with broadband spectra near nonlinear saturation levels. In acceleration-phase, the measured modulation Fourier spectra and nonlinear growth velocities are in good agreement with those predicted by Haan's model [Haan S W 1989 *Phys. Rev. A* **39** 5812]. In a real-space analysis, the bubble merger was quantified by a self-similar evolution of bubble size

distributions [Oron D *et al* 2001 *Phys. Plasmas* **8**, 2883]. The 3-D, inner-surface modulations were measured to grow throughout the deceleration phase of spherical implosions. RT growth rates are very sensitive to the drive conditions, therefore they can be used to test and validate drive physics in hydrodynamic codes used to design ICF implosions. Measured growth rates of pre-imposed 2-D target modulations below nonlinear saturation levels were used to validate non-local thermal electron transport model in laser-driven experiments.

I. INTRODUCTION

Rayleigh–Taylor (RT) instability [1,2] is of critical importance in inertial confinement fusion (ICF) [3] and astrophysics [4]. In ICF, the RT instability leads to shell disruption and performance degradation of spherically imploding targets [3]. In the linear regime of classical RT instability [3,5] small initial modulations grow exponentially in time with the growth rate $\gamma = (Akg)^{0.5}$, where k is the modulation wave number, g is the target acceleration, A is the Atwood number defined as $A = (\rho_h - \rho_l)/(\rho_h + \rho_l)$, where ρ_h and ρ_l are the densities of heavy and light fluids, respectively. Most ICF-related cases involve ablative drive, in which the growth rate $\gamma = \alpha(kg)^{0.5} - \beta k V_a$ is stabilized by the ablation term $\beta k V_a$, where V_a is the ablation velocity and α and β are constants [6,7]. The growth rates of linear RT instability have been measured in both classical [5] and ablative regimes [8-12]. The indication of nonlinearity in RT growth in real space is that the modulations develop into bubbles (penetration of the lighter fluid into the heavier) and spikes (penetration of the heavier fluid into the lighter) [13]. In Fourier space, this is equivalent to the harmonics generation of initial fundamental spatial modes. As the classical RT instability further progresses, the two fluids mix in turbulent regime [14-17]. In the case of ablative RT instability, growing modulations preserve bubble-spike shapes at the unstable interface. This allows quantitative measurements of the RT modulations in both real and Fourier space with x-ray radiography.

There are two modeling approaches for nonlinear RT instability: a modal one [18-20] that describes the evolution in Fourier space, and a bubble competition and merger approach that describes instability in real space [17,21-24]. In Fourier space, Haan's model [18] predicts that the spectral amplitudes of 3-D, broadband modulations grow exponentially with the RT growth rates of $\gamma(k)$ until they reach the saturation levels [18,25] $S_k = 2/Lk^2$ (L is the size of the analysis box), after which they grow linearly in time with the saturation velocities [18,26] $V_s(k) = S_k\gamma(k)$. The short-wavelength modes grow initially most rapidly and quickly saturate at levels S_k, while very long-wavelength modes grow more slowly. As a result, the mid-wavelength modes have the largest growth factors, producing a peak in the spectrum. As the evolution continues, this peak moves to longer wavelengths. Haan's model applies in the weakly nonlinear regime for broadband modulation amplitudes around the saturation levels [25].

In real space, bubble competition models predict that smaller bubbles (with smaller nonlinear velocities) are taken over by larger bubbles (with higher nonlinear velocities) through bubble competition and the bubble merger processes [17,21-24]. As a result, the average size of the modulations shifts to longer wavelengths as the modulations grow. The real-space models predict that the bubble sizes and amplitudes evolve with a self-similar behavior in an advanced nonlinear regime [24,27,28]. The self-similar behavior predicts that the distribution function $f\left(\lambda/\langle\lambda\rangle\right)$ of the bubble size normalized to the average bubble size $\lambda/\langle\lambda\rangle$ is constant as the modulation average size and average amplitude grow [24,27-29]. This article reviews results of Rayleigh-Taylor experiments performed over several years on the OMEGA Laser System [30]. A variety of experiments, in both acceleration-phase and deceleration-phase, with planar and spherical targets, with 2-D sinusoidal and 3-D broadband modulations are described in this article. Growth of the 3-D, broadband modulations has been presented in nonlinear regime, while the growth of 2-D sinusoidal modulations has been measured in linear regime to test and validate fundamental physics in hydrodynamic simulations. The experiments were performed with targets accelerated directly with laser light and therefore related to direct-drive ICF.

In this article, Sec. II describes the acceleration-phase RT growth measurements performed in planar targets. Section III describes the acceleration-phase RT growth measurements performed in spherically convergent targets. Section IV describes results of deceleration-phase RT growth measurements performed in spherical implosions. Section V describes the linear-growth RT measurements performed for hydro-code validation. Conclusions are presented in Sec. VI.

II. ACCELERATION-PHASE RAYLIGH-TAYLOR GROWTH IN PLANAR GEOMERTY

Figure 1 shows a schematic of acceleration-phase RT growth experiments in planar geometry [26,28]. In the experiments, initially smooth, 1-mm-diam CH targets with thicknesses ranging up to 50 μm were driven with 12-ns square pulse at laser intensities of ~5 × 10^{13} W/cm^2 with several overlapped laser beams on the OMEGA [30]. The modulation growth was measured with through-foil, x-ray radiography [29]. X-rays created in the backlighter foil driven with additional laser beams, penetrate the foil and create modulation images on a framing camera with a temporal resolution of ~80 ps and a spatial resolution of ~10 μm to be captured at different times in each shot [29]. The initial target modulations, used for these measurements, were imprinted by laser-beam nonuniformities. Figure 2 shows examples of the measured images [26] for a shot with a 50-μm-thick target driven by a 12-ns square pulse shape at 4, 6 and 10 ns. As the modulations grow, the average bubble size shifts to longer wavelengths, big bubbles become bigger, and small bubbles disappear, as is evident from the images in Fig. 2. Two to three generations of bubbles change in these images, allowing clear observations of the bubble competition and merger processes. Fourier amplitude evolution of areal-density modulations is shown in Fig. 3(a). The spectral shapes are very similar to Haan's model predictions [19]. As the evolution continues, the spectral peak moves to longer wavelengths. Comparison of the measured nonlinear velocities $V_S(k)$ with those predicted by Haan's model [26] is shown in Fig. 3(b). Excellent agreement between the experiments and the model was observed [26]. It is remarkable that a simple model predicts such complicated phenomenon as the nonlinear growth of the RT instability so accurately in terms of the spectral shapes and nonlinear velocities.

The real-space analysis of these experiments was based on evolution distributions of the bubble sizes and amplitudes along with the evolution of average bubble size and amplitude [28]. Figure 4 shows an example of the measured image with bubble edges superimposed on top of it. The evolution of the distributions of bubble sizes λ

[corresponding to images in Figs. 2(a) and 2(b)] is shown in Fig. 5(a). As modulations grow, the number of bubbles decreases while their average size and amplitude increase and the distributions become broader. The measured distributions of bubble sizes were fitted with the normal distributions from which average sizes $\langle \lambda \rangle$ were determined. Figure 5(b) shows the normalized distributions as functions of normalized bubble size $\lambda / \langle \lambda \rangle$. Bubble size distributions are in the self-similar regime because the normalized distributions do not change in time. The dashed line in Fig. 6(b) represents the fit to the experimental data using the normal distribution. The dotted and dot–dashed lines in Fig. 5(b) are the distributions predicted from the 2-D and 3-D models, respectively (presented in Ref. 27). The 3-D model prediction is in better agreement with the experimental results, as expected. In these experiments, the measured bubble-front amplitude grows as $h_b \sim 0.04\, gt^2$, as expected in a self-similar regime, where g is the foil acceleration, t is the time.

III. ACCELERATION-PHASE RAYLIGH-TAYLOR GROWTH IN SPHERICAL GEOMERTY

Figure 6 shows a schematic of the target and experimental setup for spherical RT experiments in acceleration phase [31,32]. Initially smooth, 860-μm-diam, 20- and 24-μm-thick CH shells were imploded on OMEGA [30]. The shells had 400- and 600-μm-diam openings shielded with a gold cone to prevent the laser light from entering the inner part of the spherical target. The opening made it possible for diagnostic x rays from the backlighter to radiograph one wall of the shell. The spherical targets were driven with 54 overlapped laser beams. The 54-beam drive had the same uniformity as 60-beam implosions except in the region of measurements, opposite to the shield. The backlighter x rays were produced using an additional six OMEGA beams. Experiments were performed with 3-ns square laser pulses at peak laser intensity of ~2×10^{14} W/cm^2. The modulation growth was measured with through-foil x-ray radiography [31] with the same spatial and temporal resolution as in planar-target experiments described in the previous Section. The initial target modulations used for RT growth measurements were imprinted by laser-intensity non-uniformities.

An example of measured modulation image is shown in Fig. 7(a) for the experiment with a 24-μm-thick CH shell. The central 200-μm-sq parts of the images were used to measure modulation growth and compare it with predictions of the 2-D hydrocode *DRACO* [32]. Figure 7(b) shows an example of a 2-D simulation showing shell-mass-density position and modulations (Ref. 32). The effects of the experimental spatial and temporal resolutions were included in simulations. In the simulations, the rms modulation grows ~40x from the start of the acceleration phase at 1 ns to the end of the measurements at 2.5 ns. Figure 8 compares the measured and simulated rms of areal-density modulations in these experiments. The rms areal-density amplitude grew strongly in the experiment and reached the level of ~1 mg/cm^2 at 2.5 ns, comparable to the shell's areal density at that time, significantly compromising the shell's integrity. The outer-shell convergence ratio at this time was ~2.2. Growth measurements were limited to ~2.5 ns because, at later times, the emission from the imploding target core dominated the backlighter emission, compromising the measurements. The measured and simulated modulation growths were in reasonable agreement. The *DRACO* predictions of the drive [33] and RT growth of 2-D pre-imposed modulations were also validated in planar-target experiments [34,35] at a laser intensity of ~2 × 10^{14} W/cm^2, the same intensity used in current experiments.

Experiments with planar targets, described in previous Section, showed that the average size of modulations shifts to longer wavelengths as the modulations grew in a nonlinear regime [25,26]. Smaller bubbles were absorbed by larger bubbles through bubble competition and bubble merger processes [28]. The modulation images taken at different times resembled themselves only up to the time when new generations of bubbles were created through bubble merger [28]. In convergent geometry, it was expected that the bubble merger processes became faster, compared to planar geometry, because the convergence moved bubbles closer to each other. In this case the modulation images may lose their resemblance faster in spherical geometry that in planar geometry. This effect was observed experimentally by comparing modulation evolution in planar and spherical cases. More discussion of these observations can be found in Ref. 32.

IV. DECELERATION-PHASE RAYLIGH-TAYLOR GROWTH IN SPHERICAL GEOMERTY

In deceleration phase of spherical implosions, when the hot and less dense inner gas is slowing the cold and dense shell down, inner-shell modulations grow due to deceleration-phase RT instability [3]. Unlike the acceleration-phase RT instability, where the outer-surface modulation growth is stabilized by mass ablation, the deceleration-phase RT instability is classical (for drive conditions at OMEGA), with no ablative stabilization for these targets. In the linear regime of the classical RT instability, the modulation amplitude δr_1 for mode with a wavelength of λ [$\lambda = kR$, where k is a modulation wave number and $R(t)$ is the radius, or position of the unstable surface] grows exponentially in time [3]:

$$\delta r_1 = \delta r_0 \exp\left[\sqrt{A\left(\ell/R\right) g t^2}\right], \tag{1}$$

where A is the Atwood number, δr_0 is the initial perturbation amplitude, g is the deceleration, and t is time. The characteristic of the classical RT instability is the rapid growth of short-scale perturbation that quickly enters the highly nonlinear regime causing shell density perturbations $\delta\rho$ in addition to shell amplitude perturbations δr and shell–fuel mix. The growth of longer-wavelength perturbations can be modified by the presence of mix because the mix increases the core pressure by supplying additional material into the core. As a result, the deceleration g increases and the Atwood number A decreases, modifying the shell trajectory and the modulation growth.

The other factor contributing to perturbation growth is Bell–Plesset (BP) convergent effects. As the shell converges from radius R_0 (with thickness d_0 and density ρ_0) to radius R_1 (with thickness d_1 and density ρ_1), the shell modulation δr_1 grows due to BP effects [36] as $\delta r_1 = \delta r_0 \left(\rho_0 R_0^2\right) / \left(\rho_1 R_1^2\right) = \delta r_0 d_1 / d_0$. The shell modulation due to BP growth is proportional to shell thickness: $\delta r \sim d$. Note that the modulation growth of shell integrity, $\delta[\rho d]/\rho d$, does not explicitly include BP effects $\{\delta[\rho d]/\rho d$ due to BP effects is constant because $\delta(\rho d) \sim (\rho d)\}$; however, the convergent effects constantly modify the RT instability, which is responsible for the modulation growth.

In spherical implosions near peak compression, external backlighting becomes less efficient for measurements of modulation growth because hot-core self-emission is often much stronger than external backlighting. This core emission can be used as a backlighter to probe the outer, colder shell. The modulation evolution measurements were based on differential imaging of shells with diagnostic titanium-doped layers [37-39]. Figure 9 shows experimental configuration including a pinhole array that produced images on a framing camera. The images were captured at different times below (with Ti filter) and above (using Fe filter) the titanium K-edge. Core images at photon energies below the *K* edge (not absorbed by the shell) provided the spatial shape of the backlighter, while core images at photon energies above the *K* edge (highly absorbed by the shell's titanium) contained information about the structure of shell-areal-density modulations in the titanium-doped layer. The modulations in the cold, or absorbing, part of the shell areal density $\delta[\rho d](\mathbf{r},t)$ at time t ($\mathbf{r}$ is the spatial coordinate) are proportional to the modulation in the logarithm of the ratio of intensities of the two images at photon energies above (highly absorbing by the shell) and below (weakly absorbing by the shell) the titanium *K* edge [37-40].

Figure 10 shows measured core images below (upper raw of images) and above (lower raw of images) titanium K-edge. The central images near 2.0 ns correspond to time of peak emission (that happen at peak compression) [40]. Peak neutron production was measured ~100 ps earlier than peak emission. Simultaneously, the spectral evolution of core emission was captured on an x-ray streak camera [40]. The relative areal-density modulations $\delta[\rho d]/\rho d$ in the titanium-doped layers, a measure of the shell integrity, have been obtained by normalizing the framing camera images of areal-density modulations $\delta[\rho d](\mathbf{r},t)$ to the average areal density $[\rho d](t)$ measured with the streak camera. Figure 11 presents images of measured areal-density modulations $\delta[\rho d](\mathbf{r},t)$ for the same shot as in Fig. 10, around peak compression [38]. The average titanium areal density $[\rho d](t)$ is not an accurate measure of compression in the layer because the amount of titanium atoms and ions available for absorption can be modified by the rapidly changing core radiation and the increasing temperature in the shell around peak compression. The shell integrity $\delta[\rho d]/\rho d$ is better measure since it is not affected by these effects.

Figure 12 shows the modulation growth inferred for two shots with 20-μm-thick shells and 4 atm of D^{3}He fill around peak compression [40]. The σ_{rms} of the relative areal-density modulations $\delta[\rho d]/\rho d$ grows by a factor of ~10 during the ~200 ps around peak compression. The modulation levels are ~20% at peak neutron production (~1.9 ns) and ~50% at peak compression (~2.0 ns). The shell areal density $[\rho d]$ grows by a factor of 1.5 for the same period [40] due to the growth of both the density ρ and the thickness d; therefore, the shell modulations ($\delta r \sim d$) should grow by up to a factor of 1.5 due to BP convergent effects [40]. The BP effects do not contribute directly to the growth of shell integrity, $\delta[\rho d]/\rho d$; therefore, the measured growth of relative areal-density modulation should be entirely due to the RT instability [40].

V. LINEAR-GROWTH RAYLIGH-TAYLOR MEASUREMENTS FOR CODE VALDATION

RT growth in linear regime is very sensitive to the drive conditions. Most ICF-related cases involve ablative drive, in which the growth rate $\gamma = \alpha(kg)^{0.5} - \beta k V_a$ is stabilized by the ablation term $\beta k V_a$, where V_a is the ablation velocity and α and β are constants [6,7]. By measuring the growth rates at several different spatial wavelengths, ablation velocity and acceleration can be inferred. Both acceleration of ablation velocity depend on physics of laser absorption; electron transport; and preheat due to x-rays, nonlocal and hot electrons. Therefore linear growth rate measurements can be used to test and validate crucial physics in hydrodynamic codes used to design ICF implosions.

In the linear-growth experiments [34,35], planar, 20-μm-thick CH targets were accelerated with various square pulses on the OMEGA Laser System [30] in drive intensity range from ~0.2 × 10^{15} to ~1.5 × 10^{15} W/cm^2. The target acceleration was measured using side-on radiography with a streak camera, while RT growth of pre-imposed 2-D modulations was measured with through-foil, x-ray radiography [34]. Figure 13 shows examples of the target trajectory measured with streak camera [Fig. 13(a)] and the image of 2-D modulations measured with x-ray radiography with the framing camera [35]. A primary goal of these experiments was to test local model for electron-thermal transport, used in hydro-code DRACO [33]. RT experiments at laser intensities below ~5 × 10^{14} W/cm^2 demonstrated very good agreement with simulations based on this model. Figure 14 shows RT-growth results with a 1.6-ns square drive at a laser intensity of ~5 × 10^{14} W/cm^2. Modulation growth at 60-, 30-, and 20-μm wavelengths agree well with simulations using the local model for electron-thermal transport based on the time-dependent flux limiter [34] shown in Fig. 6(c). There is a slight deviation of the predicted growth from the measured at the 20-μm wavelength, suggesting that the RT-growth stabilization starts to be observed at a drive intensity of ~5 × 10^{14} W/cm^2.

Figure 15 shows RT-growth results using the 1-ns square drive with modulations at 60-, 30-, and 20-μm wavelengths at the drive intensity of ~1 × 10^{15} W/cm^2. The 60-μm-wavelength modulations grow faster than the 30-μm perturbations, while the 20-μm-wavelength perturbations are completely stabilized [35]. The simulation predictions based on the local model show faster growth at shorter wavelengths compared to longer wavelengths. The measured stabilization of the short-wavelength modulations is consistent with an increased stabilizing term in the dispersion relation. Because the ablation velocity is inversely proportional to the density at the unstable ablation surface, the experimental data suggest that the ablation surface has been preheated. These experiments demonstrate that standard simulations based on a local model of electron thermal transport, break down at peak intensities of ignition designs (although they work well at lower intensities). Preheat by nonlocal electrons and hot electrons was suggested to explain the experiments [34,35].

Previous experiments demonstrated that nonlocal electron-thermal transport enhances the effect of ablative stabilization of the RT growth with green lasers [8,9,41,42]. The nonlocal effects become important in IR- and green-laser drives at relatively low intensities [42] of ~1×10^{14} W/cm^2, while in UV-laser drives they become important at higher intensities [33-35] of ~1×10^{15} W/cm^2. The direct-drive-ignition designs on the NIF use 351-nm UV-laser light at a peak intensity of ~1×10^{15} W/cm^2; therefore, an understanding of nonlocal effects on RT growth is critical to direct-drive ignition [34]. The standard, or local, models of electron transport [43] predict steep gradients of temperature and density near the ablation surface. The nonlocal electrons with energies >10 keV, from the tail of thermal distribution, can penetrate further into the target and cause more preheating than local models, increasing the density scale length and reducing the density at the ablation surface [44-47]. Nonlocal models [45-47] predict significant ablation-front heating when the plasma corona temperature exceeds ~3 keV.

VI. CONCLUSIONS

This article reviewed experimental results of the Rayleigh-Taylor (RT) growth experiments performed on OMEGA laser system over recent decade. The experiments were performed in acceleration phase, using planar and spherical targets, and in deceleration phase of spherical implosions, using spherical shells. In planar geometry, the nonlinear regime was studied using 3-D modulations with broadband spectra near nonlinear saturation levels. In acceleration-phase, the measured modulation Fourier spectra and nonlinear growth velocities are in good agreement with those predicted by Haan's model. In a real-space analysis, the bubble merger was quantified by a self-similar evolution of bubble size distributions. The 3-D, inner-surface modulations were measured to grow throughout the deceleration phase of spherical implosions. Measured growth rates of pre-imposed 2-D target modulations in planar targets were used to test and validate non-local thermal electron transport model in laser-driven experiments.

ACKNOWLEDGMENTS

This work was performed under the auspices of the U.S. Department of Energy by Lawrence Livermore National Laboratory under Contract DE-AC52-07NA27344.

REFERENCES

[1] Lord Rayleigh 1883 *Proc. London Math Soc.* **XIV** 170

[2] Taylor G 1950 *Proc. R. Soc. London Ser. A* **201** 192

[3] Lindl J D 1995 *Phys. Plasmas* **2** 3933

[4] Remington B A *et al* 1997 *Phys. Plasmas* **4** 1994

[5] Budil K S *et al* 1996 *Phys. Rev. Lett.* **76** 4536

[6] Takabe H *et al* 1985 *Phys. Fluids* **28** 3676

[7] Betti R *et al* 1996 *Phys. Plasmas* **3** 2122

[8] Shigemori K *et al* 1997 *Phys. Rev. Lett.* **78** 250

[9] Glendinning S G *et al* 1997 *Phys. Rev. Lett.* **78** 3318

[10] Pawley C J *et al* 1999 *Phys. Plasmas* **6** 565

[11] Knauer J P *et al* 2000 *Phys. Plasmas* **7** 338

[12] Sakaiya T *et al* 2002 *Phys. Rev. Lett.* **88** 145003

[13] Remington B A *et al* 1993 *Phys. Fluids B* **5** 2589

[14] Read K I 1984 *Physica* **12D** 45

[15] Sharp D H 1984 *Physica* **12D** 3

[16] Schneider M B, Dimonte G and Remington B 1998, *Phys. Rev. Lett.* **80** 3507

[17] Dimonte G 2004 *Phys. Rev. E* **69** 056305

[18] Haan S W 1989 *Phys. Rev. A* **39** 5812

[19] Haan S W 1991 *Phys. Fluids B* **3** 2349

[20] Ofer D, Alon U, Shvarts D, McCrory R L and Verdon C P 1996 *Phys. Plasmas* **3** 3073

[21] Gardner C L, Glimm J, McBryan O, Menikoff R, Sharp D H and Zhang Q 1988 *Phys. Fluids* **31** 447

[22] Zhang Q 1990 *Phys. Lett. A* **151** 18

[23] Glimm J and Li X L 1988 *Phys. Fluids* **31** 2077

[24] Alon U, Hecht J, Ofer D and Shvarts D 1995 *Phys. Rev. Lett.* **74** 534

[25] Smalyuk V A *et al* 1998 *Phys. Rev. Lett.* **81** 5342

[26] Smalyuk V A *et al* 2005 *Phys. Rev. Lett.* **95** 215001

[27] Oron D, Arazi L, Kartoon D, Rikanati A, Alon U and Shvarts D 2001 *Phys. Plasmas* **8** 2883

[28] Sadot O *et al* 2005 *Phys. Rev. Lett.* **95** 265001

[29] Smalyuk V A *et al* 1999 *Phys. Plasmas* **6** 4022

[30] Boehly T R *et al* 1997 *Opt. Commun.* **133** 495

[31] Smalyuk V A *et al* 2009 *Phys. Rev. Lett.* **103** 105001

[32] Smalyuk V A *et al* 2009 *Phys. Plasmas* **16** 112701

[33] Hu S X *et al* 2008 *Phys. Rev. Lett.* **103** 112701

[34] Smalyuk V A *et al* 2008 *Phys. Rev. Lett.* **101** 025002

[35] Smalyuk V A *et al* 2008 *Phys. Plasmas* **15** 082703

[36] Plesset M S and Mitchell T P 1956 *Q. Appl. Math.* **13** 419

[37] Yaakobi B *et al* 2000 *Phys. Plasmas* **7** 3727

[38] Smalyuk V A *et al* 2001 *Phys. Rev. Lett.* **87** 155002

[39] Smalyuk V A *et al* 2002 *Phys. Plasmas* **9** 2738

[40] Smalyuk V A *et al* 2003 *Phys. Plasmas* **10** 1861

[41] Azechi H *et al* 1997 *Phys. Plasmas* **4** 4079

[42] Otani K *et al* 2007 *Phys. Plasmas* **14** 122702

[43] Malone R C, McCrory R L and Morse R L 1975 *Phys. Rev. Lett.* **34** 721

[44] Bell A R, Evans R G and Nicholas D J 1981 *Phys. Rev. Lett.* **46** 243

[45] Sunahara A, Delettrez J A, Stoeckl C, Short R W and Skupsky S 2003 *Phys. Rev. Lett.* **91** 095003

[46] Colombant D G, Manheimer W M and Busquet M 2005 *Phys. Plasmas* **12** 072702

[47] Goncharov V N *et al* 2006 *Phys. Plasmas* **13** 012702

FIGURE CAPTIONS

FIG. 1. Experimental configuration for planar Rayleigh–Taylor instability experiment includes CH drive foil, a backlighter foil used to produce x-rays for x-radiography, a pinhole array that produces images on a framing camera [25]. The images are captured at different times to measure temporal evolution of Rayleigh–Taylor modulations.

FIG. 2. X-ray radiographs of the 3-D broadband modulations measured at 4, 6, and 10 ns [images (a), (b), and (c), respectively]. The bubble merger is evident in the images [26].

FIG. 3. (a) Evolution of the azimuthally averaged, areal-density modulation Fourier amplitudes as a function of spatial frequency for shots with 50-μm-thick targets driven by a 12-ns laser pulse at an intensity of ~5×10^{13} W/cm^2 from Ref. 26. The dashed line is Haan's saturation level $S_k = 2/Lk^2$ ($L = 333$ μm is the analysis-box size) multiplied by the calculated target density in order to be converted to areal density. The spectral shapes of the measured modulations are similar to those predicted by Haan's model. (b) Saturation velocities of target modulations measured at spatial frequencies of 8, 17, 33, and 50 mm^{-1}, corresponding to spatial wavelengths of 120, 60, 30, and 20 μm from Ref. 26. The dashed line is Haan's saturation velocity $V_s(k) = S_k\gamma(k)$. The measured nonlinear velocities are in excellent agreement with Haan's model predictions.

FIG. 4. An example of the measured image shows bubble edges (determined using watershed algorithm [28]) superimposed on top of it.

FIG. 5. (a) Examples of the measured bubble-size distributions in the images taken at 4 and 6 ns [images in Figs. 2(a), and 2(b), respectively] with a 50-μm-thick target driven by a 12-ns laser pulse at an intensity of ~5 × 10^{13} W/cm^2. (b) Bubble-size distributions, normalized to the total number of bubbles, as a function of the bubble size normalized to the averaged bubble size $\lambda / \langle \lambda \rangle$ for the same 4- and 6-ns images as in (a). The measured bubble distributions are in a self-similar regime because their normalized distributions do not change in time. The dashed line represents normal distribution fit to the data. Predictions of 3-D bubble competition model agree better with data than 2-D model [28].

FIG. 6. Experimental configuration for spherical Rayleigh-Taylor experiments in acceleration phase [31]. Spherical CH shells contain openings that allow diagnostic x rays from the backlighter to radiograph the shell. The gold cone serves as a shield from the laser light entering the inner part of the spherical target.

FIG. 7. (a) Central 200-μm-sq parts of the images were used to analyze the growth of the 3-D broadband modulations [32]. (b) An example of a 2-D *DRACO* simulation showing a shell mass-density contour in an experiment with a 24-μm-thick CH shell at 2.0 ns driven with a low-intensity, 3-ns square laser pulse at an intensity of ~2 × 10^{14} W/cm^2.

FIG. 8. Evolution of the simulated (solid curve) and measured (circles) areal-density rms amplitude as a function of time in experiments [32] with 24-μm-thick CH shells driven with a 3-ns pulse at an intensity of ~2 × 10^{14} W/cm^2.

FIG. 9. Experimental configuration for spherical Rayleigh-Taylor experiments in deceleration phase includes a pinhole array that produces images on a framing camera [38-40]. The images are captured at different times below (with Ti filter) and above (using Fe filter) the titanium K-edge to measure temporal evolution of Rayleigh–Taylor modulations around the time of peak compression using K-edge absorption of the titanium dopant in the CH shell [38].

FIG. 10. Core images near peak compression at energies below (~4.8 keV, upper row of images) and above (~6.5 keV, lower row of images) the titanium *K* edge for a target with a 20-μm-thick shell filled with 4 atm of D^3He gas taken at times 1.90, 1.95, 2.00, 2.05, 2.10, and 2.15 ns [40].

FIG. 11. Images of areal-density modulations for a target with a 20-μm-thick shell filled with 4 atm of D^3He gas taken at times 1.90, 1.95, 2.00, 2.05, 2.10, and 2.15 ns [40].

FIG. 12. The evolution of inner-shell relative areal-density modulation σ_{rms} as a function of time for two shots [shown by triangles and squares] with 20-μm-thick shells and 4 atm of D^3He gas [40].

FIG. 13. Examples of (a) a target-trajectory image measured with the streak camera [31] and (b) a Rayleigh–Taylor growth image of 60-μm wavelength, 2-D modulation measured with the faming camera [31] using a 3-ns square drive at a laser intensity of ~2 × 10^{14} W/cm^2.

FIG. 14. Optical-depth modulations versus time for a 1.6-ns square laser drive at an intensity of ~5 × 10^{14} W/cm^2 with wavelengths of (a) 60 μm, (b) 30 μm, and (c) 20 μm. Results of 2-D *DRACO* simulations are shown by solid curves [32].

FIG. 15. Optical-depth modulations versus time for a 1-ns square laser drive at an intensity of ~1 × 10^{15} W/cm^2 with wavelengths of (a) 60 μm, (b) 30 μm, and (c) 20 μm. Results of 2-D *DRACO* simulations are shown by solid curves [32].

Figure 1

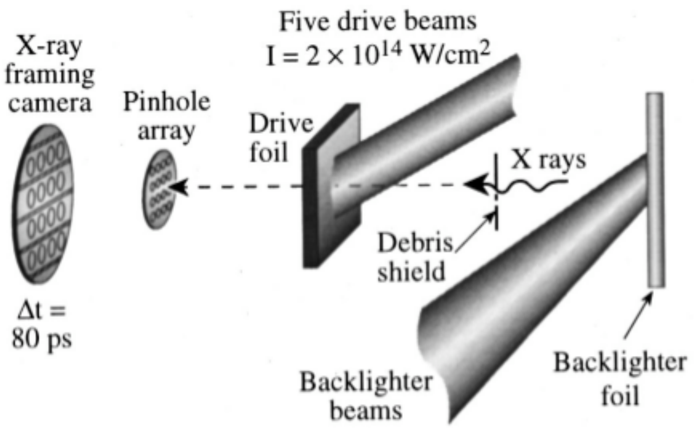
Five drive beams
I = 2 × 10^14 W/cm^2
X-ray framing camera
Pinhole array
Drive foil
X rays
Debris shield
Δt = 80 ps
Backlighter beams
Backlighter foil

Figure 2

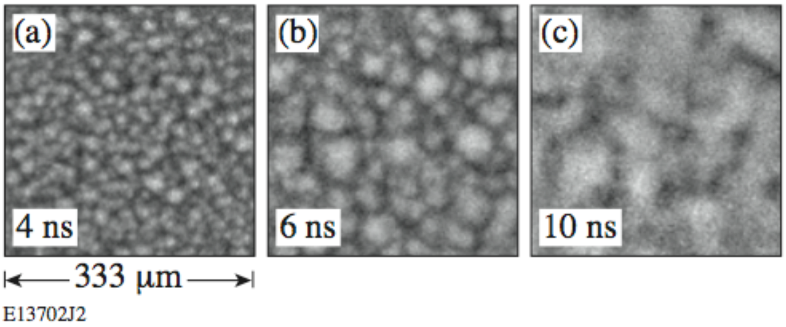

Figure 3

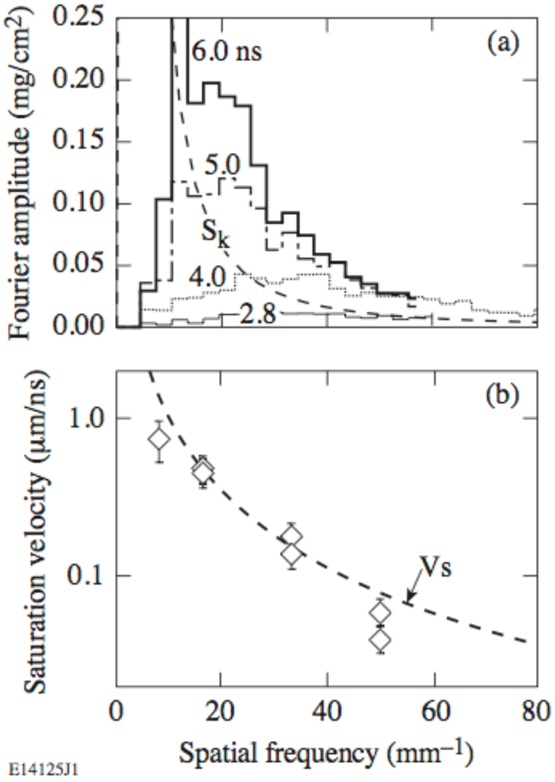

(a)
Fourier amplitude (mg/cm^2)
0.25
0.20
0.15
0.10
0.05
0.00
6.0 ns
5.0
S_k
4.0
2.8
(b)
Saturation velocity (µm/ns)
1.0
0.1
Vs
0
20
40
60
80
Spatial frequency (mm^{-1})
E14125J1

Figure 4

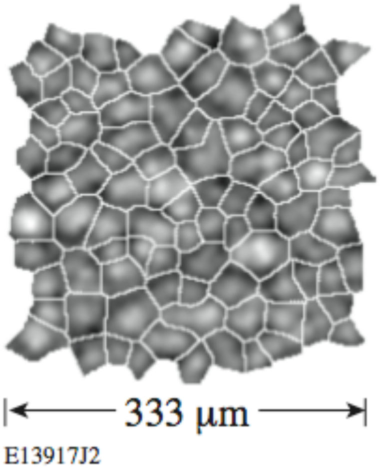

Figure 5

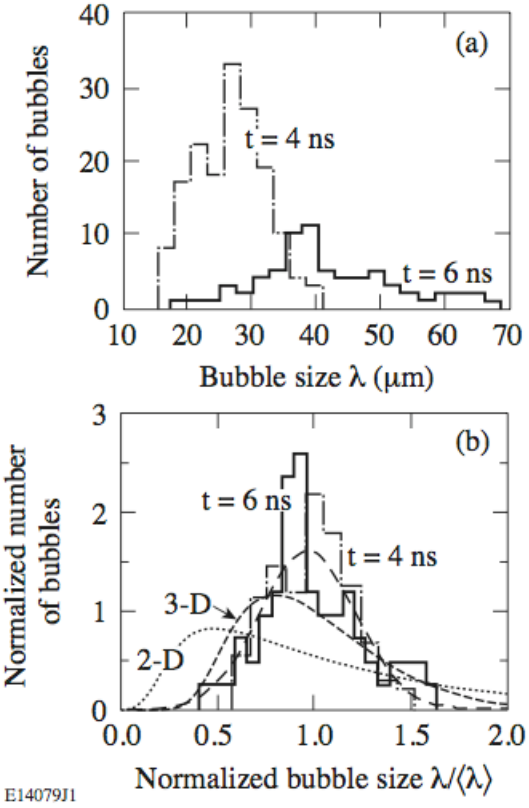
(a)
Number of bubbles
40
30
20
10
0
10
20
30
40
50
60
70
t = 4 ns
t = 6 ns
Bubble size λ (μm)
(b)
Normalized number of bubbles
3
2
1
0
0.0
0.5
1.0
1.5
2.0
t = 6 ns
t = 4 ns
3-D
2-D
Normalized bubble size λ/⟨λ⟩
E14079J1

Figure 6

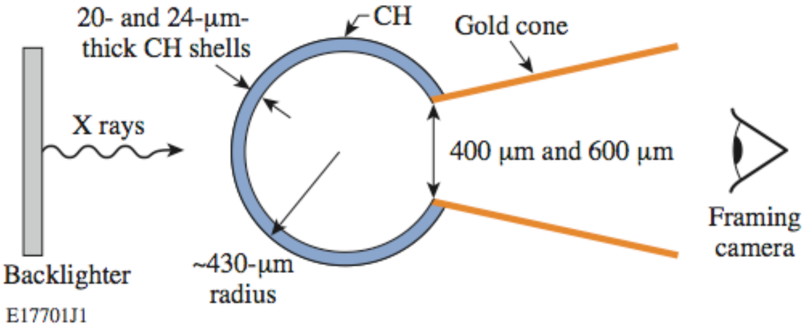
20- and 24-μm-
thick CH shells
CH
Gold cone
X rays
400 μm and 600 μm
Framing
camera
Backlighter
~430-μm
radius
E17701J1

Figure 7

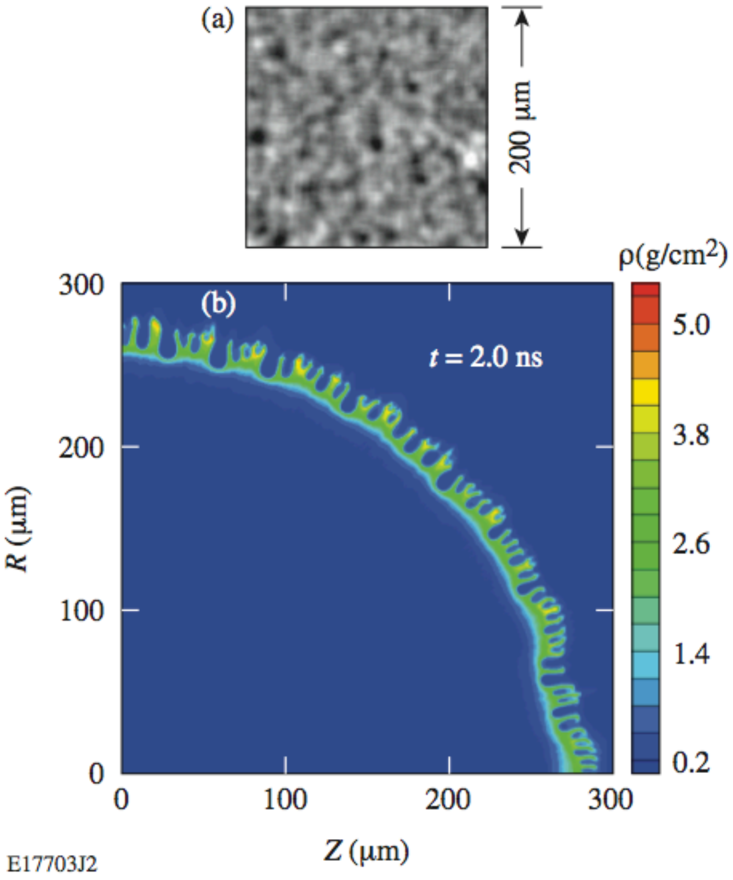
(a)
200 μm
(b)
t = 2.0 ns
ρ(g/cm2)
5.0
3.8
2.6
1.4
0.2
300
200
100
0
R (μm)
0
100
200
300
Z (μm)
E17703J2

Figure 8

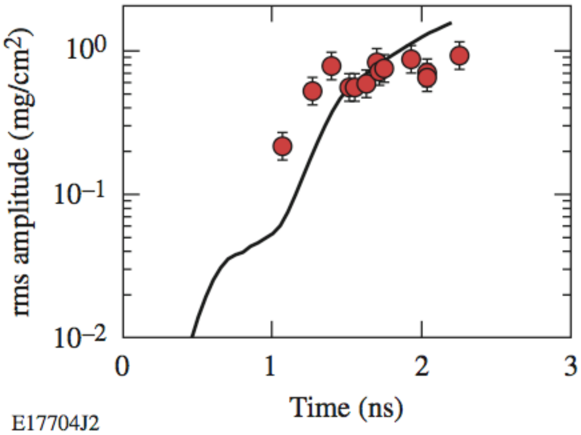

Figure 9

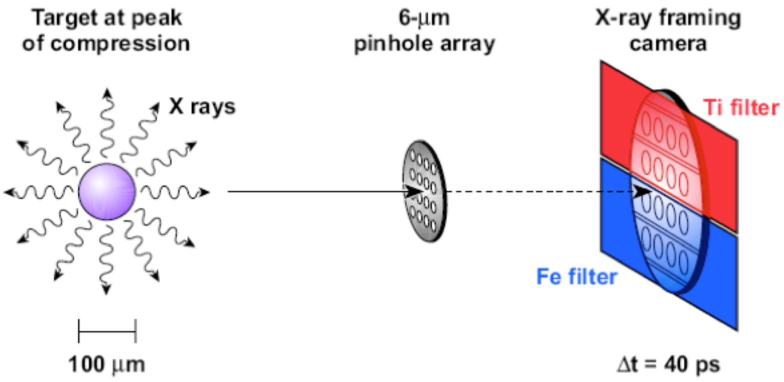
Target at peak of compression
6-μm pinhole array
X-ray framing camera
X rays
Ti filter
Fe filter
100 μm
Δt = 40 ps

Figure 10

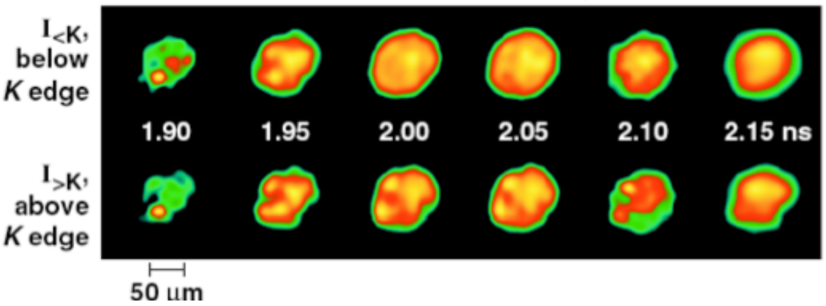

Figure 11

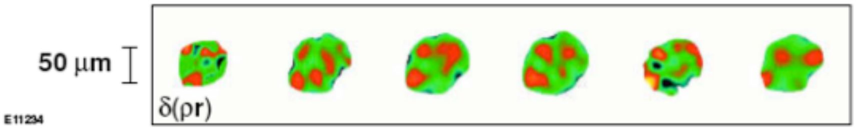

Figure 12

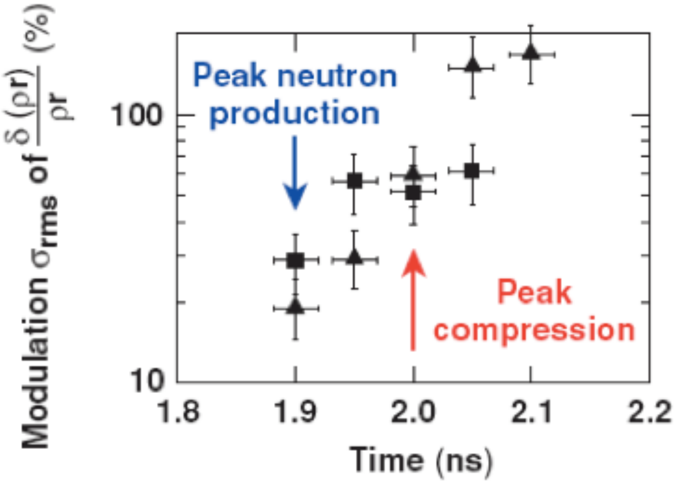

Modulation σ_{rms} of $\frac{\delta(\rho r)}{\rho r}$ (%)
100
10
1.8
1.9
2.0
2.1
2.2
Time (ns)
Peak neutron production
Peak compression

Figure 13

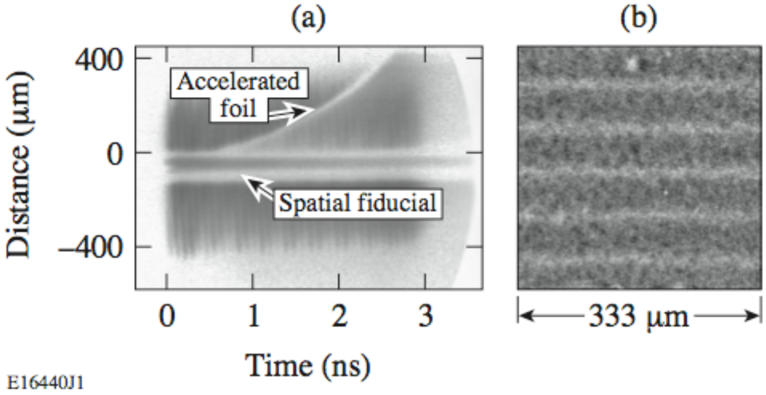
(a)
(b)
400
0
–400
Distance (μm)
Accelerated foil
Spatial fiducial
0
1
2
3
Time (ns)
333 μm
E16440J1

Figure 14

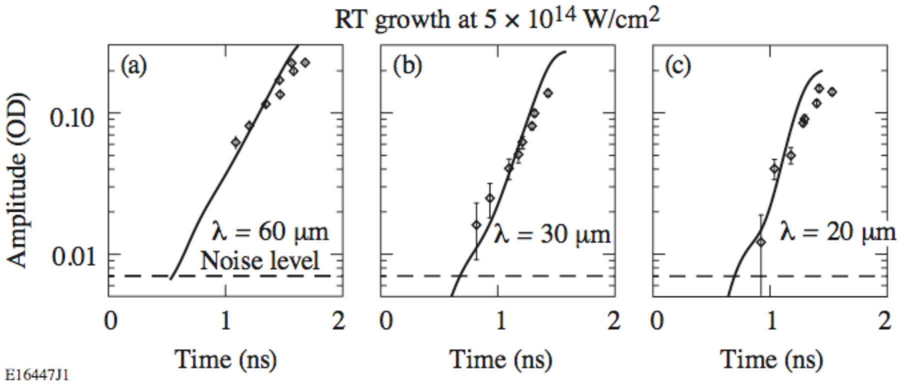
RT growth at 5 × 10^14 W/cm^2
Amplitude (OD)
0.10
0.01
(a)
λ = 60 μm
Noise level
(b)
λ = 30 μm
(c)
λ = 20 μm
0
1
2
Time (ns)
E16447J1

Figure 15

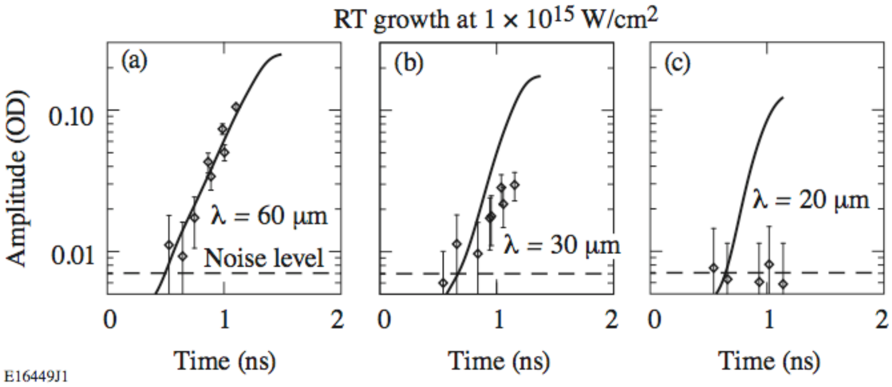
RT growth at 1 × 10^15 W/cm^2
(a)
(b)
(c)
Amplitude (OD)
0.10
0.01
λ = 60 μm
Noise level
λ = 30 μm
λ = 20 μm
0
1
2
Time (ns)
E16449J1